

# Spectroscopic Properties and Quantum Chemistry-Based Normal Coordinate Analysis (QCB-NCA) of a Dinuclear Tantalum Complex Exhibiting the Novel Side-On End-On Bridging Geometry of N<sub>2</sub>: Correlations to Electronic Structure and Reactivity

Felix Studt,<sup>†</sup> Bruce A. MacKay,<sup>‡</sup> Michael D. Fryzuk,<sup>‡</sup> and Felix Tuczek<sup>\*,†</sup>

Contribution from the Institut für Anorganische Chemie, Christian Albrechts Universität Kiel, Ohlshausenstrasse 40, 24098 Kiel, Germany, and Department of Chemistry, University of British Columbia, Vancouver, B.C., V6T 1Z1 Canada

Received July 1, 2003; E-mail: ftuczek@ac.uni-kiel.de

**Abstract:** The vibrational properties and the electronic structure of the side-on end-on N<sub>2</sub>-bridged Ta complex ([NPN]Ta( $\mu$ -H))<sub>2</sub>( $\mu$ - $\eta^1$ : $\eta^2$ -N<sub>2</sub>) (**1**) (where [NPN] = (PhNSiMe<sub>2</sub>CH<sub>2</sub>)<sub>2</sub>PPh) are analyzed. Vibrational characterization of the Ta<sub>2</sub>( $\mu$ -N<sub>2</sub>)( $\mu$ -H)<sub>2</sub> core is based on resonance Raman and infrared spectroscopies evaluated with a novel quantum chemistry-based normal coordinate analysis (QCB-NCA). The N–N stretching frequency is found at 1165 cm<sup>-1</sup> exhibiting a <sup>15</sup>N<sub>2</sub> isotope shift of –37 cm<sup>-1</sup>. Four other modes of the Ta<sub>2</sub>N<sub>2</sub>H<sub>2</sub> core are observed between 430 and 660 cm<sup>-1</sup>. Two vibrations of the bridging hydrido ligands are also identified in the spectra. On the basis of experimental frequencies and the QCB-NCA procedure, the N–N force constant is determined to be 2.430 mdyne Å<sup>-1</sup>. The Ta–N force constants are calculated to be 2.517 mdyne Å<sup>-1</sup> for the Ta– $\eta^1$ -N<sub>2</sub> bond and 1.291 and 0.917 mdyne Å<sup>-1</sup> for the Ta– $\eta^2$ -N<sub>2</sub> bonds, respectively. DFT calculations on **1** suggest that the bridging dinitrogen ligand carries a charge of –1.1, which is equally distributed over the two nitrogen atoms. However, orbital analysis reveals that the terminal nitrogen makes lower contributions to the  $\pi$  orbitals and much higher contributions to the  $\pi^*$  orbitals of the N<sub>2</sub> ligand than the bridging nitrogen. This suggests that reactions of the dinitrogen ligand with electrophiles should preferentially occur at the terminal N atom, in agreement with experimental results.

## Introduction

Developing metal-based systems that can coordinate and functionalize molecular nitrogen (N<sub>2</sub>) is a challenging but important area of research.<sup>1</sup> Currently there are a number of efforts focused on the use of N<sub>2</sub> as a feedstock to produce higher-value organonitrogen products.<sup>2–5</sup> What makes this challenging is that this simple, readily available diatomic molecule is intrinsically inert and is not a particularly good ligand. However, when it can be induced to bind to a metal complex, dinitrogen is said to be activated and the extent of this activation is an important feature that may correlate to functionalization.<sup>6</sup> Measures of activation are generally gauged by N–N bond lengths as established by X-ray crystallography and by N–N stretching frequencies obtained from infrared and Raman spectroscopies.<sup>7,8</sup> An in-depth understanding of the

bonding in these complexes can then be developed by normal coordinate analysis (NCA) coupled with DFT calculations.<sup>9</sup>

On the basis of the lengthening of the N–N bond for coordinated N<sub>2</sub>, the highest levels of activation are generally found for complexes of the early transition elements and some lanthanide derivatives.<sup>1,10</sup> These complexes typically feature dinitrogen units bridging at least two metal centers. The most common bridging modes are (i) end-on bridging with N–N bond lengths in the range 1.2–1.3 Å and N–N stretching frequencies of about 1200–1300 cm<sup>-1</sup>,<sup>11,12</sup> and (ii) side-on bridging with N–N bond lengths of approximately 1.5 Å and N–N stretching frequencies of 700–800 cm<sup>-1</sup>.<sup>13–15</sup> We previously reported a

<sup>†</sup> Christian Albrechts Universität Kiel.

<sup>‡</sup> University of British Columbia.

- (1) Fryzuk, M. D.; Johnson, S. A. *Coord. Chem. Rev.* **2000**, *200–202*, 379–409.
- (2) Hidai, M. *Coord. Chem. Rev.* **1999**, *185–186*, 99–108.
- (3) Akashi, M.; Sato, Y.; Mori, M. *J. Org. Chem.* **2001**, *66*, 7873–7874.
- (4) Yandulov, D. V.; Schrock, R. R.; Rheingold, A. L.; Ceccarelli, C.; Davis, W. M. *Inorg. Chem.* **2003**, *42*, 796–813.
- (5) Mori, M.; Hori, K.; Akashi, M.; Hori, M.; Sato, Y.; Nishida, M. *Angew. Chem., Int. Ed.* **1998**, *37*, 636.
- (6) Tuczek, F.; Lehnert, N. *Angew. Chem., Int. Ed.* **1998**, *37*, 2636–2638.

- (7) Tuczek, F.; Horn, K. H.; Lehnert, N. *Coord. Chem. Rev.* **2003**, *245*, 107–120.
- (8) Smith, J. M.; Lachicotte, R. J.; Pittard, K. A.; Cundari, T. R.; Lukat-Rodgers, G.; Rodgers, K. R.; Holland, P. L. *J. Am. Chem. Soc.* **2001**, *123*, 9222–9223.
- (9) Horn, K. H.; Lehnert, N.; Tuczek, F. *Inorg. Chem.* **2003**, *42*, 1076–1086.
- (10) Gambarotta, S. *J. Organomet. Chem.* **1995**, *500*, 117–26.
- (11) Cohen, J. D.; Mylvaganam, M.; Fryzuk, M. D.; Loehr, T. M. *J. Am. Chem. Soc.* **1994**, *116*, 9529.
- (12) Fryzuk, M. D.; Haddad, T. S.; Mylvaganam, M.; McConville, D. H.; Rettig, S. J. *J. Am. Chem. Soc.* **1993**, *115*, 2782.
- (13) Fryzuk, M. D.; Haddad, T. S.; Rettig, S. J. *J. Am. Chem. Soc.* **1990**, *112*, 8185.
- (14) Cohen, J. D.; Fryzuk, M. D.; Loehr, T. M.; Mylvaganam, M.; Rettig, S. J. *Inorg. Chem.* **1998**, *37*, 112.
- (15) Fryzuk, M. D.; Love, J. B.; Rettig, S. J.; Young, V. G. *Science (Washington, D.C.)* **1997**, *275*, 1445–1447.

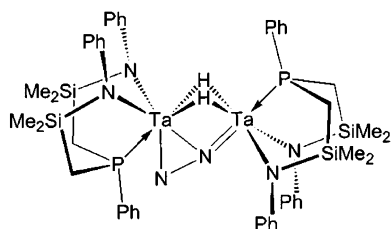


Figure 1. Structure of **1**.

spectroscopic characterization of the  $Zr_2N_2$  core in the dinuclear Zr complex  $([P_2N_2]Zr)_2(\mu-\eta^2:\eta^2-N_2)$  (where  $[P_2N_2] = PhP(CH_2SiMe_2NSiMe_2CH_2)_2PPh$ ) (**2**), which exhibits the side-on bridging geometry for  $N_2$ . In the Raman spectrum the N–N stretch was found at  $775\text{ cm}^{-1}$ .<sup>16</sup> On the basis of this vibration and three other modes of the  $Zr_2N_2$  core observed in Raman and IR spectra, a quantum chemistry-assisted normal coordinate analysis (QCA-NCA) was performed. The force constants for the N–N and Zr–N bonds were calculated to be 1.53 and 2.58 mdyn  $\text{\AA}^{-1}$ , respectively.

Herein we describe a similar detailed Raman and IR study of the recently characterized diamagnetic complex  $([NPN]Ta(\mu-H)_2(\mu-\eta^1:\eta^2-N_2))$  (where  $[NPN] = (PhNSiMe_2CH_2)_2PPh$ ), **1**, which contains  $N_2$  bound in an unprecedented side-on end-on bridging mode (cf. Figure 1).<sup>17</sup> The N–N internuclear distance of 1.32  $\text{\AA}$  suggests lower activation than is exhibited in the side-on derivative studied previously. However, this unusual bonding arrangement has already led to new reactions for coordinated dinitrogen including hydroboration<sup>18</sup> and hydrosilylation.<sup>19</sup> As before, vibrational data are evaluated by normal coordinate analysis (NCA). Conventional NCA, however, is precluded for **1** because its low symmetry ( $C_s$  in room-temperature solution and  $C_1$  in the solid state) leads to a large number of off-diagonal elements in the f-matrix. In response to this, a new quantum chemistry-based normal coordinate analysis (QCB-NCA) method has been developed to fully treat the experimental data. This is related to the QCA-NCA procedure employed before in vibrational studies on dinitrogen complexes.<sup>9,16,20,21</sup> However, in contrast to QCA-NCA, where only the largest matrix elements of the f-matrix were retained, the new QCB-NCA method uses the *full* f-matrix obtained from the DFT calculation without imposing any simplifications. In the last step, selected force constants in this matrix are fitted to match the frequencies of those modes that have been experimentally assigned. This procedure represents a powerful and generally applicable new method to treat the vibrational properties of large molecules, by combining the information available from DFT calculations with experimental results to a maximum degree.

On the basis of the DFT calculation, the electronic structure of **1** is described and its electronic transitions are determined. These predictions are compared to the electronic absorption spectrum, allowing assignment of prominent features in the UV–vis spectrum. Finally, the implications of the electronic

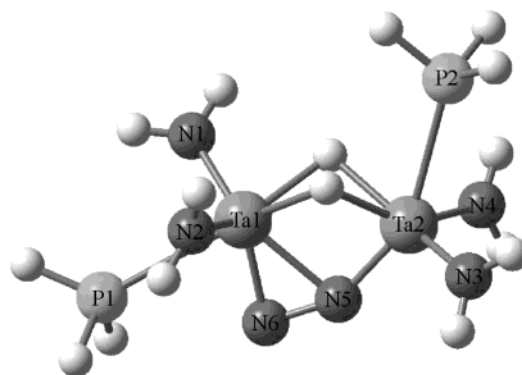


Figure 2. Structure of the optimized model **I**.

structure of **1** are analyzed with respect to its reactivity patterns, particularly its ability to undergo electrophilic additions.

## Results and Analysis

**1. Vibrational Spectroscopic Analysis.** Raman and infrared spectroscopies were applied to **1** and its  $^{15}N$ - and  $(\mu-D)_2$ -enriched isotopomers, respectively. Spectroscopic data were evaluated with a quantum chemistry-based normal coordinate analysis (QCB-NCA). This procedure involves an ab initio calculation of vibrational frequencies to aid in spectral analysis and the generation of an f-matrix that subsequently is employed in normal coordinate analysis (see below). A model of **1** is shown in Figure 2 (model **I**). The structure has approximate  $C_s$  symmetry with a mirror plane going through Ta1, Ta2, N5, and N6. On the basis of optimization of this model in  $C_1$  symmetry, DFT frequency calculations were performed. The results are collected in Table 1 together with theoretical potential energy distributions (PEDs) and measured frequencies. The  $Ta_2(\mu-H)_2(\mu-\eta^1:\eta^2-N_2)$  core of **1** is expected to have  $3 \times 6 - 6 = 12$  vibrations: four Ta–H stretches and one H–Ta–H bend of the  $Ta_2(\mu-H)_2$  unit, four in-plane vibrations and one out-of-plane (with respect to the mirror plane of **1**) vibration of the  $Ta_2(\mu-\eta^1:\eta^2-N_2)$  unit, one out-of-plane bending motion between the  $(\mu-H)_2$  and the  $(\mu-\eta^1:\eta^2-N_2)$  units, and one Ta–Ta stretch. In agreement with this prediction, the DFT frequency calculation gives five modes for the  $Ta_2N_2$  unit which correspond to one N–N stretching mode, one  $Ta_2\eta^1-N_2$  mode, two  $Ta_1\eta^2-N_2$  vibrations (symmetric and asymmetric), and one out-of-plane mode of the dinitrogen unit. The eigenvectors (normal modes) of these vibrations are shown in Figure 3. The calculations also predict six modes for the  $Ta_2H_2$  moiety designated  $\nu(Ta-H)1 - \nu(Ta-H)6$ , the eigenvectors (normal modes) of which are given in Figure 4. As apparent from this figure, the H–Ta–H bending motion is not present as a pure normal coordinate but mixes with the four Ta–H stretches, and the out-of-plane bending motion between the  $(\mu-H)_2$  and the  $(\mu-N_2)$  units  $\nu(Ta-H)6$  primarily involves H motion. The Ta–Ta stretch, finally, is also distributed over a number of modes.

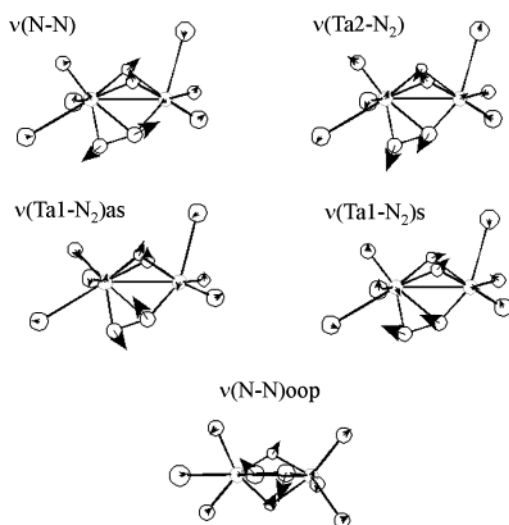
Solid-state resonance Raman spectra and infrared spectra of **1** as well as its  $^{15}N$ - and  $(\mu-D)_2$ -labeled isotopomers are shown in Figures 5, 6, and 7. The resonance Raman spectra were recorded at an excitation wavelength of 568.2 nm, which provides strong resonance enhancement to the vibrations of the  $Ta_2(\mu-H)_2(\mu-\eta^1:\eta^2-N_2)$  core of **1**. On the basis of the DFT-calculated frequencies and isotope shifts, the experimentally observed vibrations are assigned: the N–N stretching band was

- (16) Studt, F.; Morello, L.; Lehnert, N.; Fryzuk, M. D.; Tuzcek, F. *Chem. Eur. J.* **2003**, *9*, 520.  
 (17) Fryzuk, M. D.; Johnson, S. A.; Patrick, B. O.; Albinati, A.; Mason, S. A.; Koetzle, T. F. *J. Am. Chem. Soc.* **2001**, *123*, 3960–3973.  
 (18) Fryzuk, M. D.; MacKay, B. A.; Johnson, S. A.; Patrick, B. O. *Angew. Chem., Int. Ed.* **2002**, *41*, 3709–3712.  
 (19) Fryzuk, M. D.; MacKay, B. A.; Patrick, B. O. *J. Am. Chem. Soc.* **2003**, *125*, 3234–3235.  
 (20) Habeck, C. M.; Lehnert, N.; Naether, C.; Tuzcek, F. *Inorg. Chim. Acta* **2002**, *337*, 11–31.  
 (21) Lehnert, N.; Tuzcek, F. *Inorg. Chem.* **1999**, *38*, 1659–1670.

**Table 1.** Calculated Frequencies of Model System **1** and Assignments of the Observed Features in the Spectra of Complex **1**: Potential Energy Distribution of **1** Derived from the DFT Calculation

mode	B3LYP			experimental <sup>d</sup>			PED (B3LYP) [%] <sup>a</sup>							
	<sup>14</sup> N	<sup>15</sup> N	<sup>2</sup> H	<sup>14</sup> N	<sup>15</sup> N	<sup>2</sup> H	N–N		Ta–N		Ta–H		Ta–ligand	
$\nu(\text{N–N})$	1119	1082	1117	1165	1128	1162	60.8		30.2		0.8		0.1	
$\nu(\text{Ta2–N}_2)$	651	633	648	656	636 643	644	0.1		74.4		1.2		9.6	
$\nu(\text{Ta1–N}_2)_{\text{as}}$	610 594	583	591	625	603	607	3.5 1.2	7.7 <sup>b</sup>	18.3 7.4	42.4 <sup>b</sup>	2.0 0.4	0.6 <sup>b</sup>	56.4 81.7	9.9 <sup>b</sup>
$\nu(\text{Ta1–N}_2)_{\text{s}}$	482	470	479	487	482 463	485 463	10.1		53.3		6.0		4.1	
$\nu(\text{N–N})_{\text{oop}}$	464	452	455	442	432	435	1.8		55.1		2.7		2.0	
$\nu(\text{Ta–H})_1$	1495	1495	1062	n.o.	n.o.	1080	0.0		0.0		62.8		0.0	
$\nu(\text{Ta–H})_2$	1355	1355	963	n.o.	n.o.	974	0.0		0.0		64.5		0.0	
$\nu(\text{Ta–H})_3$	1140	1140	819	n.o.	n.o.	n.o.	0.0		0.1		61.6		0.1	
$\nu(\text{Ta–H})_4$	991	991	740	n.o.	n.o.	n.o.	0.0		0.2		52.4		0.2	
$\nu(\text{Ta–H})_5$	981	981	713	n.o.	n.o.	n.o.	0.6		0.5		59.8		0.5	
$\nu(\text{Ta–H})_6$	751	751	517	n.o.	n.o.	n.o.	0.0		0.8		4.2 <sup>c</sup>		12.1	

<sup>a</sup> PED of the unlabeled compound. <sup>b</sup> PED of the <sup>15</sup>N-substituted compound. <sup>c</sup> This mode has 82.5% H bending distribution in the PED. <sup>d</sup> Raman data. n.o. = not observed.

**Figure 3.** Eigenvectors of the five modes of the  $\text{Ta}_2\text{N}_2$  unit (DFT B3LYP). The arrows correspond to unit displacements of normal coordinates with a scaling factor of 2.

calculated to be at  $1119\text{ cm}^{-1}$ , exhibiting <sup>15</sup>N and deuterium isotope shifts of  $^{15}\Delta = -37\text{ cm}^{-1}$  and  $^{\text{D}}\Delta = -2\text{ cm}^{-1}$ , respectively. Since the only isotope-sensitive feature in this region of the Raman and IR spectra is an intense peak at  $1165\text{ cm}^{-1}$  ( $^{15}\Delta = -37\text{ cm}^{-1}$ ;  $^{\text{D}}\Delta = -3\text{ cm}^{-1}$ ), this feature is straightforwardly assigned to the N–N stretching mode  $\nu(\text{N–N})$ . The end-on terminal  $\text{N}_2$ -to-Ta2 stretch ( $\nu(\text{Ta2–N}_2)$  mode) was calculated at  $651\text{ cm}^{-1}$  ( $^{15}\Delta = -18\text{ cm}^{-1}$ ;  $^{\text{D}}\Delta = -3\text{ cm}^{-1}$ ) and is found at  $656\text{ cm}^{-1}$ , shifting to a double-peak feature at  $643$  and  $636\text{ cm}^{-1}$  in the Raman spectrum of the <sup>15</sup>N-labeled isotopomer. Splitting of this feature probably is due to mixing of the <sup>15</sup>N-shifted vibration with terminal Ta–ligand modes (cf. the contribution of Ta–ligand in the PED of  $\nu(\text{Ta2–N}_2)$ , Table 1). Averaging of the position of the two peaks in the <sup>15</sup>N spectrum gives a frequency of  $639.5\text{ cm}^{-1}$ , corresponding to an isotope shift of  $-16.5\text{ cm}^{-1}$  for  $\nu(\text{Ta2–N}_2)$ , which fits quite well to the predicted value of  $-18\text{ cm}^{-1}$ . There is another isotope-sensitive peak located at  $668\text{ cm}^{-1}$  ( $^{15}\Delta = -4\text{ cm}^{-1}$ ;  $^{\text{D}}\Delta = -3\text{ cm}^{-1}$ ). This feature is probably a terminal Ta–ligand mode as well, which acquires isotope sensitivity from small contributions of  $\nu(\text{Ta2–N}_2)$ .

Contributions from terminal Ta–ligand modes are also

present in the calculations for the asymmetric  $\text{Ta1–}\eta^2\text{-N}_2$  vibration, as they predict a splitting of this mode into two peaks at  $610$  and  $594\text{ cm}^{-1}$ , which, upon <sup>15</sup>N substitution, shift into a single feature at  $583\text{ cm}^{-1}$  (this mixing is also evident from the PEDs given in Table 1). Upon deuterium substitution, it is predicted that these two peaks merge into a single feature at  $591\text{ cm}^{-1}$ . Averaging of the frequencies of the two <sup>14</sup>N vibrations at  $610$  and  $594\text{ cm}^{-1}$  results in a calculated <sup>15</sup>N isotope shift of  $-19$  and a calculated <sup>2</sup>H shift of  $-11\text{ cm}^{-1}$ . On the basis of this result, the peak at  $625\text{ cm}^{-1}$  ( $^{15}\Delta = -22\text{ cm}^{-1}$ ;  $^{\text{D}}\Delta = -18\text{ cm}^{-1}$ ) found in the Raman and IR spectra of **1** is assigned to  $\nu(\text{Ta1–N}_2)_{\text{as}}$ . As a consequence of these assignments, mixing of the terminal Ta–ligand modes is not evident in the spectroscopic data for  $\nu(\text{Ta1–N}_2)_{\text{as}}$  but instead in the splitting of  $\nu(\text{Ta2–N}_2)$  (vide supra). Therefore these ligand modes appear to be at slightly higher frequencies than in the DFT calculation, i.e., at  $\sim 640\text{ cm}^{-1}$  instead of  $\sim 600\text{ cm}^{-1}$ .

The symmetric  $\nu(\text{Ta1–N}_2)_{\text{s}}$  stretching mode is calculated to be at  $482\text{ cm}^{-1}$  ( $^{15}\Delta = -12\text{ cm}^{-1}$ ;  $^{\text{D}}\Delta = -3\text{ cm}^{-1}$ ). In this spectral region the Raman spectra of **1** show two isotope-sensitive peaks at  $487\text{ cm}^{-1}$  ( $^{15}\Delta = -5\text{ cm}^{-1}$ ;  $^{\text{D}}\Delta = -2\text{ cm}^{-1}$ ) and  $469\text{ cm}^{-1}$  ( $^{15}\Delta = -6\text{ cm}^{-1}$ ;  $^{\text{D}}\Delta = -6\text{ cm}^{-1}$ ). Since the overall <sup>15</sup>N isotope shift as well as the average location of the two peaks fits well to the DFT predictions, these peaks are assigned to  $\nu(\text{Ta1–N}_2)_{\text{s}}$ . It is, however, not clear whether the observed splitting occurs via mixing with terminal Ta–ligand modes (vide supra) or by mixing with Ta–H modes since both  $\nu(\text{Ta–ligand})$  and  $\nu(\text{Ta–H})$  are calculated to be at higher energy. Finally, the out-of-plane mode  $\nu(\text{N–N})_{\text{oop}}$  is calculated to be at  $464\text{ cm}^{-1}$  ( $^{15}\Delta = -12\text{ cm}^{-1}$ ;  $^{\text{D}}\Delta = -9\text{ cm}^{-1}$ ) and is found at  $442\text{ cm}^{-1}$  ( $^{15}\Delta = -10\text{ cm}^{-1}$ ;  $^{\text{D}}\Delta = -7\text{ cm}^{-1}$ ) in the Raman spectra of **1**.

As mentioned above, the calculations predict six vibrational modes for the  $\text{Ta}_2\text{H}_2$  moiety (see Figure 4 and Table 1, respectively).  $\nu(\text{Ta–H})_1$  is calculated to be at  $1495\text{ cm}^{-1}$ , shifting down to  $1062\text{ cm}^{-1}$  upon substitution with deuterium. There is a peak at  $1080\text{ cm}^{-1}$  in the Raman and IR spectra of the deuterium-labeled isotopomer which does not appear in the spectra of unlabeled **1** and fits quite well with the theoretical prediction for the <sup>2</sup>H shifted vibration  $\nu(\text{Ta–H})_1$  (Figures 5 and 6). The <sup>1</sup>H counterpart appears to be in the region of  $1580\text{ cm}^{-1}$ , where it mixes with other modes. These features exhibit small

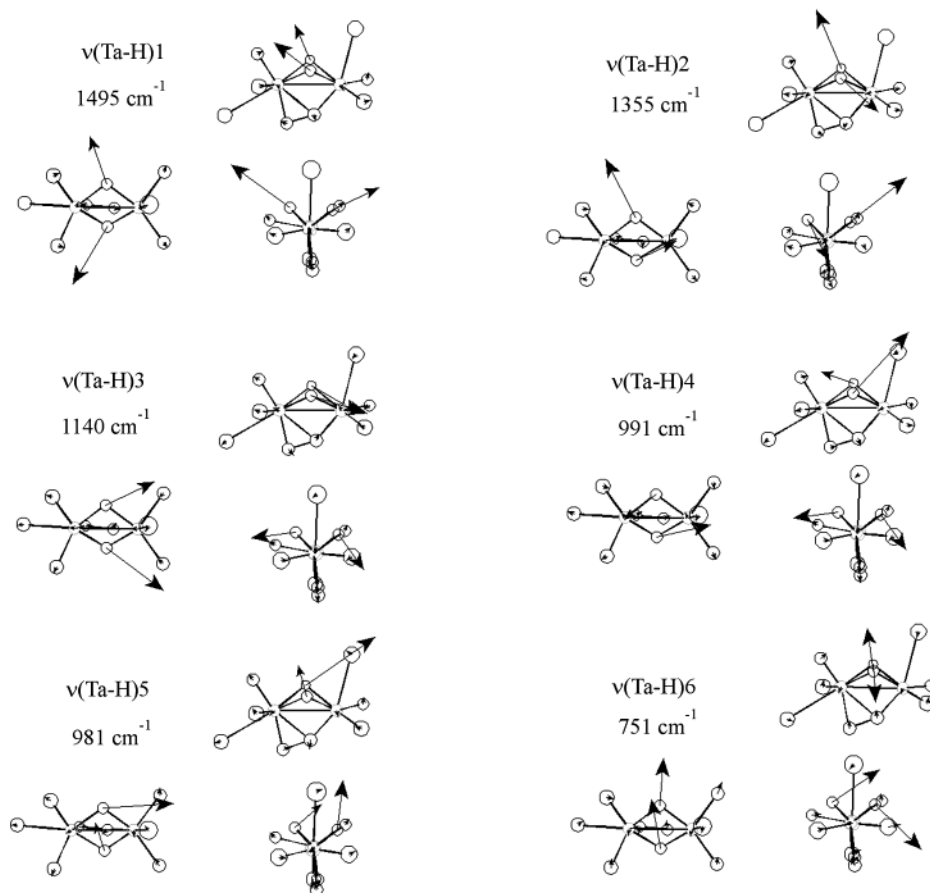


**Figure 4.** Eigenvectors and frequencies of the six modes of the  $\text{Ta}_2\text{H}_2$  unit (DFT B3LYP). The arrows correspond to unit displacements with a scaling factor of 2.

isotope shifts in both the Raman and IR spectra upon deuteration of the bridging hydride ligands. The same applies to  $\nu(\text{Ta-H})_2$ , which is clearly observed only in the Raman and IR spectra of the deuterium-labeled isotopomer at  $974\text{ cm}^{-1}$  (Figures 5 and 6). The  $^1\text{H}$  counterpart is not visible in the Raman spectrum and is masked in the IR spectrum by a cluster of peaks around  $1480\text{ cm}^{-1}$ , which also exhibit small isotope shifts. The four other Ta–H modes predicted by DFT calculations (see Figure 4 and Table 1, respectively) are not observed in the spectra. Instead, additional peaks appear at  $737, 687, 628, 592, 537, 529, 511,$  and  $426\text{ cm}^{-1}$  in the deuterium-labeled Raman spectrum of **1**. These features probably derive from mixing of ligand modes with modes of the  $\text{Ta}_2\text{H}_2$  moiety and thus receive their intensity through contribution from  $\text{Ta}_2\text{H}_2$  modes.

**2. Quantum Chemistry-Based Normal Coordinate Analysis (QCB-NCA).** To analyze the vibrational properties of complex **1**, a QCB-NCA has been applied. This is a new version of the quantum chemistry-assisted normal coordinate analysis (QCA-NCA) that has been developed earlier to account for the vibrational properties of mononuclear dinitrogen complexes of Mo and W.<sup>7,21</sup> In contrast to QCA-NCA, however, QCB-NCA uses the full  $f$ -matrix generated from the GAUSSIAN frequency calculation for NCA treatment. The QCB-NCA procedure is particularly useful for the treatment of large molecules with normal coordinate analysis if (a) the symmetry of the molecule is low (e.g.,  $C_1$ ), so that this lack of symmetry leads to a large number of different diagonal and off-diagonal elements which cannot be neglected, (b) only a small number of frequencies as compared to the total number of degrees of freedom of the whole

system can safely be assigned, and (c) only these few vibrations as well as their force constants are of interest. In the following, the separate steps of QCB-NCA are explained. The procedure is shown in Figure 8 as a flowchart.

First, the frequencies of the optimized model are calculated by DFT. The  $f$ -matrix that derives from this calculation has its force constants in Cartesian coordinates. These Cartesian coordinates from the Gaussian output are transformed into internal coordinates by using the program Redong.<sup>22</sup> The resulting  $f'$ -matrix in internal coordinates is put unchanged into the force constant fit program FFIT. In a last step, only a few force constants of interest are fit to match the observed experimental frequencies and isotope shifts whereby all other diagonal and off-diagonal elements of the  $f'$ -matrix are fixed to their theoretically calculated values. Thus, no force constants are neglected during the QCB-NCA procedure, in contrast to QCA-NCA, where only the largest force constants are retained.

To apply the QCB-NCA procedure to compound **1**, model **I** (see Figure 2) was used for the DFT calculation of the theoretical force field. In the course of the QCB-NCA procedure the hydrogen atoms of the  $\text{NH}_2$  and  $\text{PH}_3$  groups were removed to avoid artificial interactions. The resulting model **I'** is shown in Figure 9. Since only the vibrational modes of the  $\text{Ta}_2\text{N}_2$  and the  $\text{Ta}_2\text{H}_2$  units are of interest, only the force constants for these moieties were fit to experimental values. The three Ta–N ( $r_{\text{TaN}1} - r_{\text{TaN}3}$ ), the N–N ( $r_{\text{NN}}$ ), and the four Ta–H ( $r_{\text{TaH}1} - r_{\text{TaH}4}$ ) distances were used as internal coordinates (see Figure 9). The

(22) Allouche, A.; Pourcin, J. *Spectrochim. Acta.* **1993**, *49A*, 571.

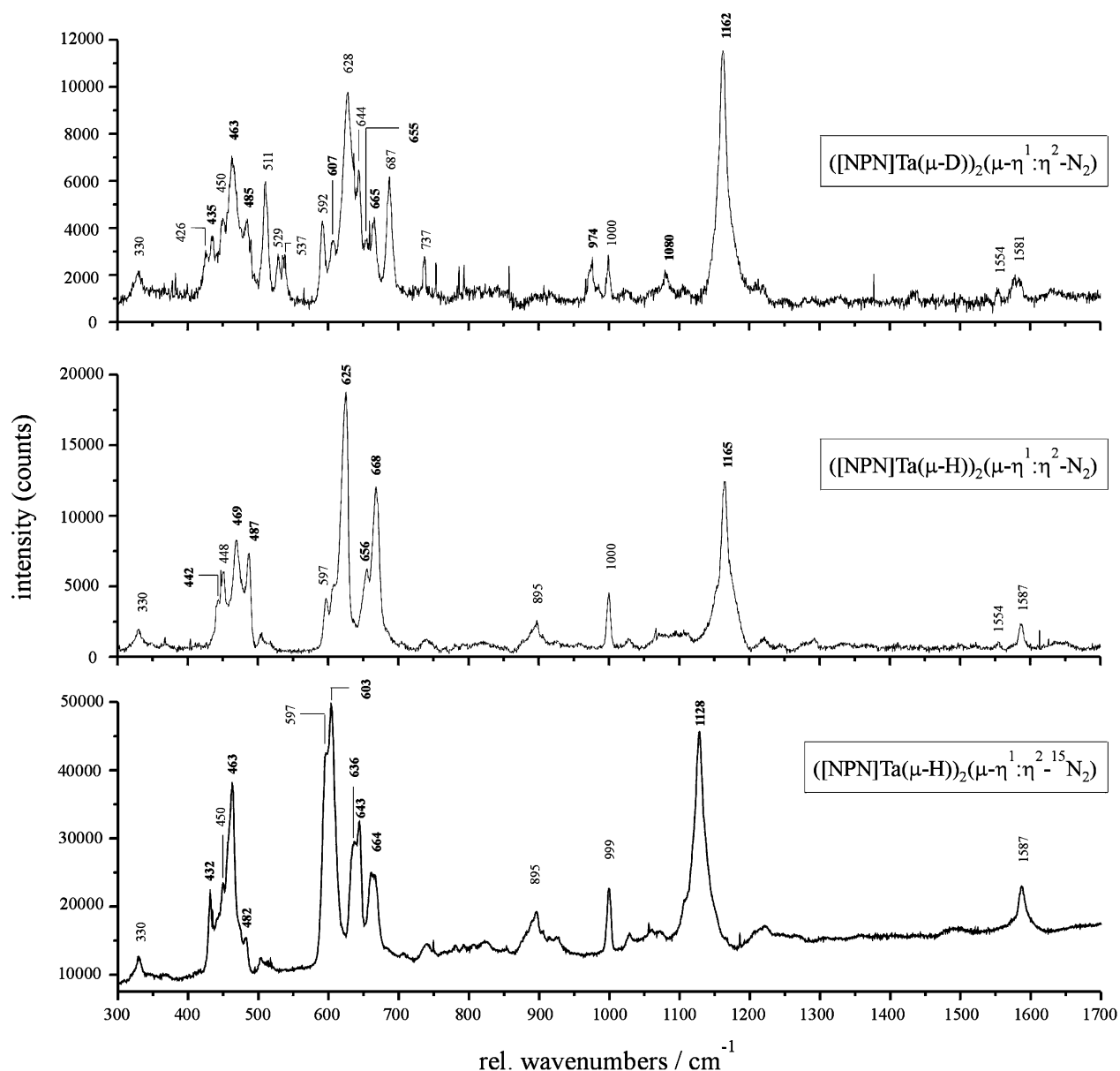


**Figure 5.** Raman spectra of **1** recorded with an excitation wavelength of 568.2 nm at 10 K.

out-of-plane internal coordinate of N6 ( $\gamma_{\text{NN}}$ ) was introduced for the description of the out-of-plane mode  $\gamma(\text{N}-\text{N})_{\text{oop}}$ . The bond lengths and angles of the N and P terminal ligands as well as the angles of the  $\text{Ta}_2\text{N}_2\text{H}_2$  core and the corresponding force constants were fixed at their theoretical values derived from the DFT calculation. Apart from a few off-diagonal elements of the  $\text{Ta}_2\text{N}_2$  unit designated a–f, all other off-diagonal elements were fixed at their calculated DFT values. The resulting f-matrix is shown in Scheme 1. The 15 different force constants were fit to the observed frequencies.

Comparison of the experimental frequencies and the frequencies resulting from QCB-NCA shows overall good agreement, as evident from inspection of Table 2. The force field obtained for the  $\text{Ta}_2\text{N}_2\text{H}_2$  core is given in Table 3. The force constant of the N–N stretch is  $2.430 \text{ mdyn } \text{\AA}^{-1}$ . The force constant for the end-on-coordinated  $\text{Ta}_2\text{-N}_5$  stretch ( $r_{\text{TaN}3}$ ) is calculated to be  $2.517 \text{ mdyn } \text{\AA}^{-1}$ , whereas the force constants for the side-on coordination  $r_{\text{TaN}1}$  and  $r_{\text{TaN}2}$  are  $1.291$  and  $0.917 \text{ mdyn } \text{\AA}^{-1}$ , respectively. As expected from consideration of relative bond lengths, the end-on coordination is the strongest Ta–N bond

of **1**, whereas the side-on  $\text{Ta}_1\text{-N}_2$  force constants are weaker. Moreover, the side-on coordination is significantly stronger for the terminal nitrogen atom than for the bridging nitrogen atom, which is also reflected by the shorter Ta–N distance for the terminal nitrogen atom as compared to the bridging one. The interaction between the three different force constants  $r_{\text{NN}}$ ,  $r_{\text{TaN}1}$ , and  $r_{\text{TaN}2}$  is significant, as can be seen from the values of the off-diagonal elements of the  $\text{Ta}_1\text{-N}_2$  core (see Table 3). Finally, the force constant for the out-of-plane mode  $\gamma_{\text{N-N}}$  is calculated to be  $0.482 \text{ mdyn } \text{\AA}^{-1}$ , and the force constants for the  $\text{Ta}_2\text{H}_2$  moiety are in the range  $0.688\text{--}0.427 \text{ mdyn } \text{\AA}^{-1}$ .

**3. Electronic Structure and UV–Vis Spectroscopic Properties.** To correlate the spectroscopic properties of **1** with its electronic structure, the MO scheme of **1** is briefly described in this section. On the basis of the MO diagram, the UV–vis absorption bands of **1** are assigned. For simplification of the DFT calculation, the [NPN] ligands of **1** were replaced by monodentate  $\text{NH}_2$  and  $\text{PH}_3$  groups. The resulting model  $([\text{PH}_3](\text{NH}_2)_2\text{Ta}(\mu\text{-H}))_2(\mu\text{-}\eta^1:\eta^2\text{-N}_2)$  (**I**) (see Figure 2) was

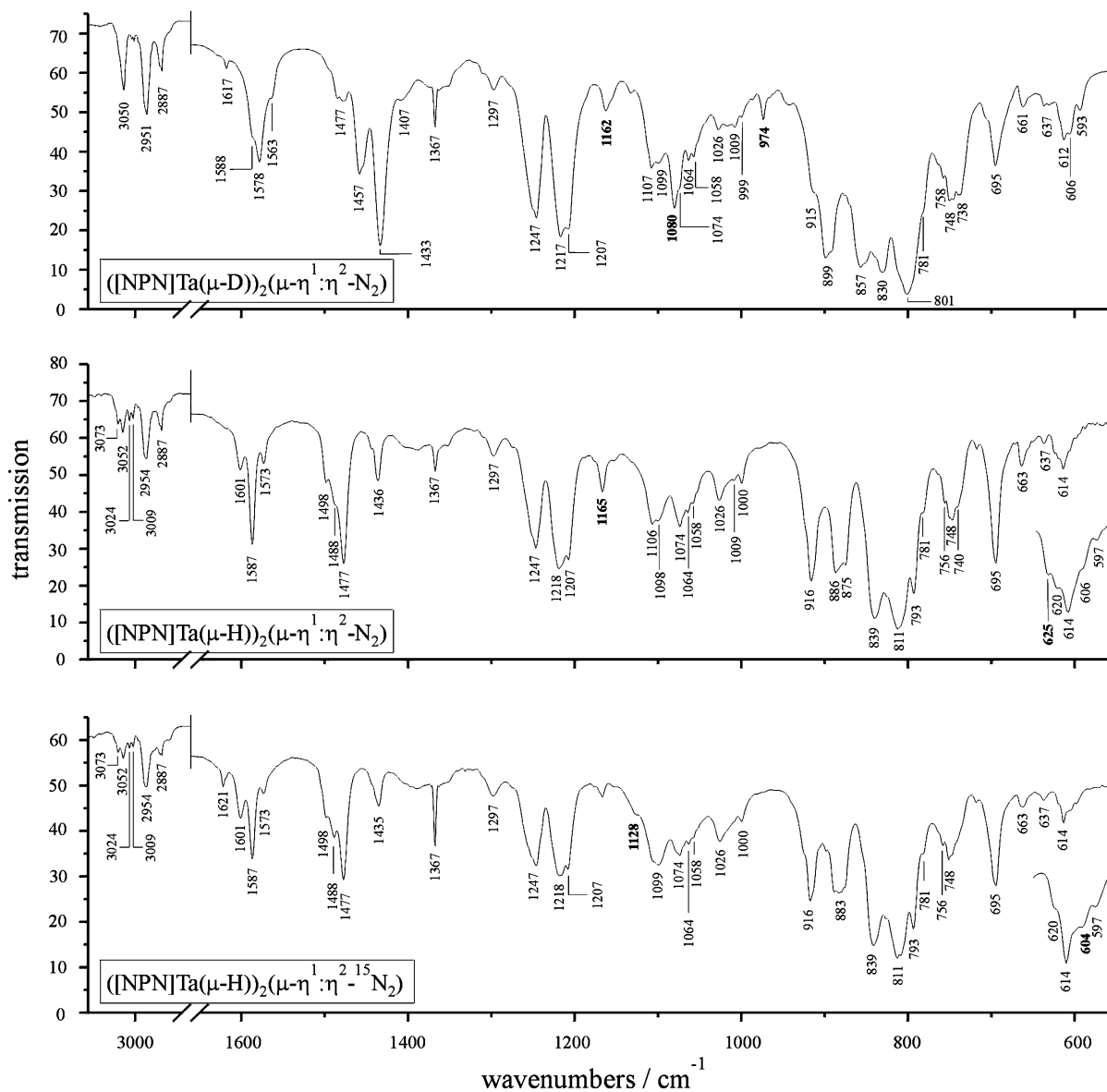


Figure 6. MIR spectra of **1** at 10 K.

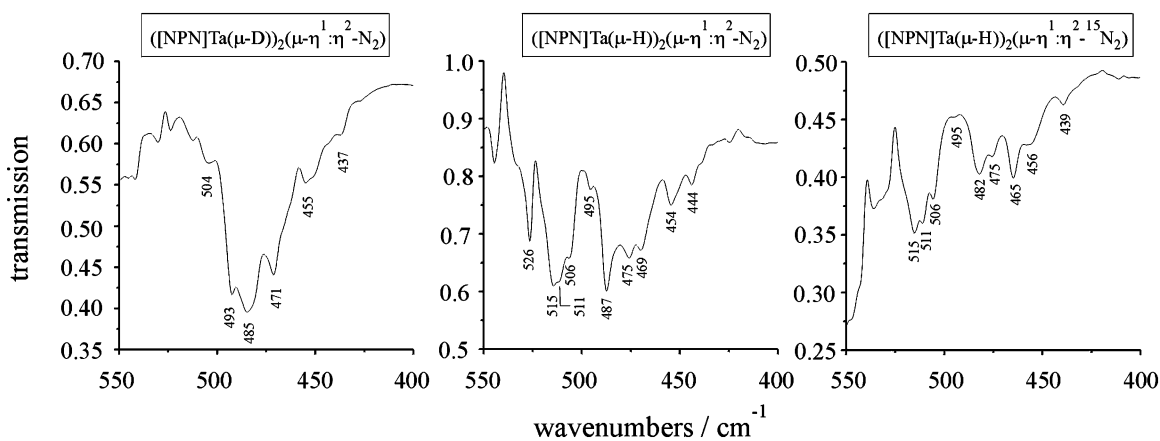


Figure 7. Far-IR spectra of **1** at 10 K.

optimized in  $C_1$  symmetry (vide supra). Restrictions were imposed on the Ta–Ta–N–H dihedral angles. These were intended to reproduce the steric constraints of the [NPN] ligand,

which prevents the amido donors from rotating freely. This model has been used before for an MO analysis of **1**.<sup>17</sup>

Figure 10 shows a section of the molecular orbital diagram

Scheme 1. f-Matrix

	$r_{NN}$	$r_{TaN1}$	$r_{TaN2}$	$r_{TaN3}$	$\gamma_{N-N}$	$r_{TaH1}$	$r_{TaH2}$	$r_{TaH3}$	$r_{TaH4}$	...
$r_{NN}$	$r_{NN}$									
$r_{TaN1}$	a	$r_{TaN1}$								
$r_{TaN2}$	b	c	$r_{TaN2}$							
$r_{TaN3}$	d	e	f	$r_{TaN3}$						
$\gamma_{N-N}$					$\gamma_{N-N}$					
$r_{TaH1}$						$r_{TaH1}$				
$r_{TaH2}$							$r_{TaH2}$			
$r_{TaH3}$								$r_{TaH3}$		
$r_{TaH4}$									$r_{TaH4}$	
...										

fixed by GAUSSIAN

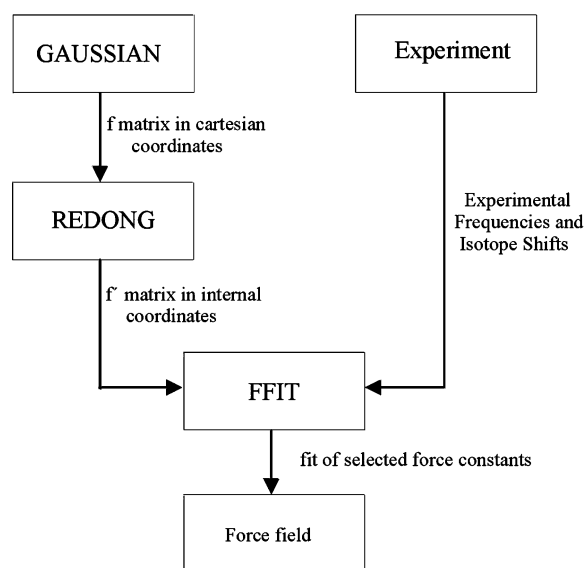


Figure 8. Flowchart of the QCB-NCA procedure.

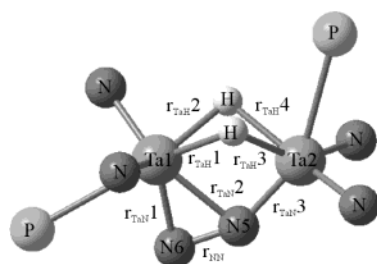


Figure 9. Internal coordinate definitions of model I used for QCB-NCA calculation.

Table 2. Comparison of the Observed Frequencies for Complex 1 with the QCB-NCA Results of Model I

mode	experimental			QCB-NCA		
	$^{14}\text{N}$	$^{15}\text{N}$	D	$^{14}\text{N}$	$^{15}\text{N}$	D
$\nu(\text{N-N})$	1165	1128	1162	1166	1127	1165
$\nu(\text{Ta2-N}_2)$	656	636	644	656	640	638
		643				
$\nu(\text{Ta1-N}_2)_{\text{as}}$	625	603	607	625	603	613
$\nu(\text{Ta1-N}_2)_{\text{s}}$	487	482	485	479	466	475
	469	463	463			
$\nu(\text{N-N})_{\text{oop}}$	442	432	435	444	430	434
$\nu(\text{Ta-H})_1$	n.o.	n.o.	1080	1520	1520	1080
$\nu(\text{Ta-H})_2$	n.o.	n.o.	974	1371	1371	974

of I; contour plots and charge contributions are given in Figure 11 and Table 4, respectively. The model is oriented such that the  $x$ -axis is along the Ta-Ta vector and the  $y$ -axis lies within the  $\text{Ta}_2\text{N}_2$  plane. The  $\pi_v$  and  $\pi_v^*$  orbitals of the dinitrogen ligand

Table 3. Force Constants of the Internal Coordinates of the  $\text{Ta}_2\text{N}_2\text{H}_2$  Core

internal coordinate	force constant <sup>a</sup>	internal coordinate	force constant <sup>a</sup>
$r_{NN}$	2.430	$r_{TaH4}$	0.427
$r_{TaN1}$	1.291	$a$	0.576
$r_{TaN2}$	0.917	$b$	0.586
$r_{TaN3}$	2.517	$c$	0.651
$\gamma_{N-N}$	0.482	$d$	0.292
$r_{TaH1}$	0.688	$e$	0.038
$r_{TaH2}$	0.477	$f$	0.122
$r_{TaH3}$	0.442		

<sup>a</sup> Units are  $\text{mdyn \AA}^{-1}$ .

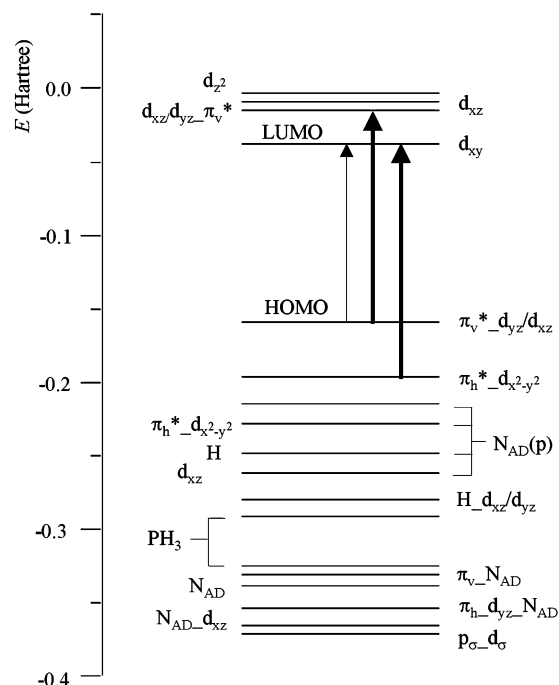


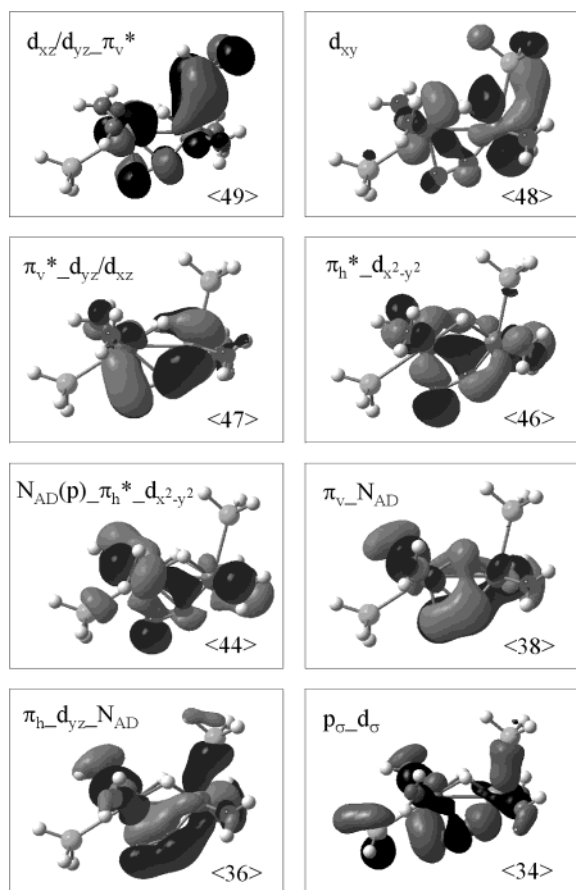
Figure 10. MO diagram of model I. MO designations correspond to those in Table 4.

are vertical ( $v$ ) to this plane, whereas the  $\pi_h$  and  $\pi_h^*$  orbitals are lying within this plane (horizontal,  $h$ ). The HOMO  $\pi_v^*_d_{yz}/d_{xz}$  (47) has a dominant nitrogen character and derives from the bonding combination of the  $\pi_v^*$  function of dinitrogen and the mixed  $d_{yz}/d_{xz}$  orbitals of the metal centers to form  $\pi$  bonds to Ta1 and Ta2. The interaction between the in-plane  $\pi^*$  orbital  $\pi_h^*$  and  $d_{x^2-y^2}$  results in two  $\sigma$  bonds between N5/N6 and Ta1 and one  $\pi$  bond between N5 and Ta2. The corresponding orbital  $\pi_h^*_d_{x^2-y^2}$  (46), HOMO-1) has 36% nitrogen character. The orbitals of the amido lone pairs of the  $\text{NH}_2$  groups are found

**Table 4.** Charge Contributions of Model I<sup>a</sup>

orbital	label	energy [hartree]	charge decomposition [%]						
			Ta1d	Ta2d	N6	N5	( $\mu$ -H) <sub>2</sub> <sup>b</sup>	N <sub>AD</sub> <sup>b,c</sup>	P <sup>b</sup>
d <sub>z</sub> <sup>2</sup>	51	-0.00317	24	17	3	7	2	8	10
d <sub>xz</sub>	50	-0.00947	13	11	5	3	3	10	27
d <sub>xz</sub> /d <sub>yz</sub> - $\pi_v^*$	49	-0.01502	13	8	8	9	1	3	19
d <sub>xy</sub>	48	-0.03827	21	30	1	2	0	3	16
$\pi_v^*$ -d <sub>yz</sub> /d <sub>xz</sub>	47	-0.15904	11	28	30	13	3	6	1
$\pi_h^*$ -d <sub>x<sup>2</sup>-y<sup>2</sup></sub>	46	-0.19668	16	6	26	10	2	32	4
N <sub>AD</sub> (p)	45	-0.21409	4	3	2	2	4	80	3
N <sub>AD</sub> (p)- $\pi_h^*$ -d <sub>x<sup>2</sup>-y<sup>2</sup></sub>	44	-0.22763	10	4	14	4	0	55	6
N <sub>AD</sub> (p)-H	43	-0.24772	6	3	1	5	11	64	2
N <sub>AD</sub> (p)-d <sub>xz</sub>	42	-0.26115	3	15	3	0	1	73	0
H-d <sub>xz</sub> /d <sub>yz</sub>	41	-0.27984	10	4	7	4	23	19	22
PH <sub>3</sub>	40	-0.29105	8	1	6	4	9	21	40
PH <sub>3</sub>	39	-0.32505	8	3	6	8	3	6	54
$\pi_v$ -N <sub>AD</sub>	38	-0.33092	4	4	12	25	1	39	1
N <sub>AD</sub>	37	-0.33852	4	7	7	11	6	39	5
$\pi_h$ -d <sub>yz</sub> -N <sub>AD</sub>	36	-0.35349	9	7	12	25	1	31	6
N <sub>AD</sub> -d <sub>xz</sub>	35	-0.36498	7	12	3	6	2	57	1
p <sub><math>\sigma</math></sub> -d <sub><math>\sigma</math></sub>	34	-0.37116	6	9	27	21	0	14	8

<sup>a</sup> Only selected orbitals are listed. <sup>b</sup> The charge decomposition gives the sum of all contributions of the corresponding atoms. <sup>c</sup> N<sub>AD</sub> is the nitrogen atom of the NH<sub>2</sub> group.

**Figure 11.** Contour plots of important molecular orbitals of I.

between <42> and <45> and mix with other orbitals, in particular those of the N<sub>2</sub> unit. Especially N<sub>AD</sub>(p)- $\pi_h^*$ -d<sub>x<sup>2</sup>-y<sup>2</sup></sub> (<44>) has a strong participation of  $\pi_h^*$ -d<sub>x<sup>2</sup>-y<sup>2</sup></sub> (see Table 4 and Figure 11). By summation of the nitrogen contributions of <44> and <46> the nitrogen character of  $\pi_h^*$ -d<sub>x<sup>2</sup>-y<sup>2</sup></sub> increases to 54%. Hence both  $\pi^*$  orbitals of N<sub>2</sub> are occupied, leading to a significant reduction of the dinitrogen unit. It should be noticed that this transfer of charge from the metals to the dinitrogen unit is much

**Table 5.** NPA Charges of Model System I

atom	charge	atom	charge <sup>a</sup>
Ta(1)	1.42	H	-0.22
Ta(2)	1.28	N <sub>AD</sub> H <sub>2</sub>	-0.41
N(6)	-0.55	PH <sub>3</sub>	0.22
N(5)	-0.53		

<sup>a</sup> Charge for each atom; charges are averaged.

more pronounced for the terminal nitrogen than for the bridging one (see Table 4).

Importantly, the  $\pi$  orbitals of dinitrogen also interact with the tantalum d functions. Specifically,  $\pi_h$  interacts with the d<sub>yz</sub> function of Ta2 to form a  $\pi$  bond. Since this orbital has about 16% metal d character, this corresponds to a transfer of charge from dinitrogen to tantalum. The same applies to the interaction of  $\pi_v$  with the metal centers; however, the charge transfer is lower than for  $\pi_h$ . Moreover, the transfer of charge from the dinitrogen to the metals is much higher for the terminal nitrogen than for the bridging one. This decreases the negative charge and the charge asymmetry of the N<sub>2</sub> unit inferred from the analysis of  $\pi_v^*$  and  $\pi_h^*$  (vide supra). Finally, the orbital p <sub>$\sigma$</sub> -d <sub>$\sigma$</sub> , which derives from a bonding combination of the  $\sigma$  bonding function of dinitrogen and a d <sub>$\sigma$</sub>  metal orbital, is  $\sigma$  bonding to Ta2, whereas the interaction with Ta1 is quite weak and can be described as a  $\pi$  bond.

The LUMOs have strong participations from tantalum d orbitals, corresponding to an approximate Ta(V) configuration (d-shell empty). The LUMO itself (<48>) is a pure metal d<sub>xy</sub> function having no nitrogen contribution. The next higher orbital, d<sub>xz</sub>/d<sub>yz</sub>- $\pi_v^*$  (<49>), is the antibonding combination of the  $\pi_v^*$  function of dinitrogen and d<sub>xz</sub>/d<sub>yz</sub>. Since both back-bonding  $\pi^*$  orbitals of N<sub>2</sub> are filled and at lower energy than the manifold of d functions (vide supra), an inverted bonding situation applies to the dinitrogen ligand as in the dinuclear side-on N<sub>2</sub>-bridged Zr complex **2**.<sup>16</sup>

Table 5 summarizes the atomic charges for the optimized model I calculated by the natural population analysis (NPA). In the inverted bonding scheme, up to four electrons are transferred from the tantalum atoms to the  $\pi^*$  orbitals of the dinitrogen ligand, which therefore becomes strongly reduced.

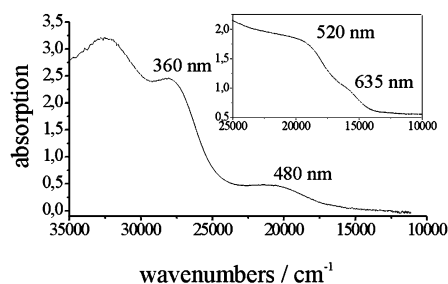


**Figure 12.** UV-vis spectrum of **1** in diethyl ether (room temperature). Inset: Solid-state spectrum (neat compound) at 10 K.

On the other hand, charge donation from the dinitrogen ligand to the metals via its  $\pi$  and  $p_\sigma$  orbitals (vide supra) decreases this negative charge to  $-1.08$ , the charge being distributed equally over both nitrogen atoms. Conversely, due to charge donation from the amide donor orbitals, the bridging hydrido ligands, and the negatively charged dinitrogen moiety to the metals, the  $+5$  charges of the Ta atoms are reduced to  $+1.42$  and  $+1.28$ , respectively. The  $-1.08$  charge of  $N_2$  resulting from NPA appears to be in contrast to the N–N bond length and stretching frequency of **1**, which are more compatible with a diazenido ( $N_2^{2-}$ ) description. This discrepancy can be explained by the fact that both effects contributing to the net charge of  $-1.08$ , the transfer of electron density from the metals to the  $\pi^*$  orbitals and the donation from the  $\pi$  orbitals to the metal atoms, cause a weakening of the N–N bond, leading to an increase of the N–N distance and a decrease of the N–N stretching frequency.

The UV-vis spectra of complex **1** (Figure 12) exhibit two characteristic absorptions at 360 and 500 nm. Furthermore, there is an additional absorption at 635 nm that is quite weak and is only observed in the solid-state UV-vis absorption spectrum. As there is no band of lower energy, this band is assigned to the lowest-energy transition of **1**, which, based on the MO scheme of **1** (see Figure 10), corresponds to the HOMO–LUMO transition. Since the HOMO  $\pi_{v^*}^*_{d_{yz}/d_{xz}}$  has 43% nitrogen contribution and the LUMO  $d_{xy}$  has 51% tantalum d character, this feature corresponds to an  $N_2$ -to-Ta charge transfer (CT) transition. As the overlap between the out-of-plane  $d_{yz}/d_{xz}$  and the in-plane  $d_{xy}$  orbitals is rather small, the intensity of this absorption is weak. The two intense features in the UV-vis spectrum are assigned to the ligand-to-metal CT (LMCT) transitions from the HOMO  $\pi_{v^*}^*_{d_{yz}/d_{xz}}$  to  $d_{xz}/d_{yz}$ - $\pi_{v^*}^*$  and from  $\pi_{h^*}^*_{d_{x^2-y^2}}$  to the LUMO  $d_{xy}$ , respectively. These transitions are higher in energy than the HOMO–LUMO transition and, since the overlap of the corresponding orbitals is large, are also more intense. As these CT transitions occur via transfer of an electron from  $N_2$ -metal bonding to nonbonding orbitals and removal of an electron from the  $\pi^*$  orbitals of the dinitrogen, the excited state should exhibit a shortening of the N–N bond and a lengthening of Ta–N distances. Thus, the vibrations of the  $Ta_2N_2$  core should be enhanced upon irradiation at about 500 nm. This agrees with the resonance enhancement of these modes observed upon irradiation at 568 nm.

## Discussion

In the preceding sections spectroscopic properties of the side-on end-on  $N_2$  complex **1** were determined. Vibrational spectroscopic (Raman/IR) and UV-vis absorption data were evaluated with the help of DFT calculations, allowing the correlation

of the spectroscopic properties of **1** with its electronic structure. In the vibrational data of complex **1** (resonance Raman and IR spectra) all four in-plane normal modes plus the out-of-plane mode of the  $Ta_2N_2$  unit were observed. The N–N stretching band was found at  $1165\text{ cm}^{-1}$  having a  $^{15}N$  isotope shift of  $-37\text{ cm}^{-1}$ . The  $Ta_2$ - $N_2$  mode was observed at  $656\text{ cm}^{-1}$  in the Raman spectrum, shifting down into a broad feature of two bands at  $636$  and  $643\text{ cm}^{-1}$ . As the calculations also predict the Ta-ligand modes of the amides to be in this region, the splitting of  $\nu(Ta_2-N_2)$  probably occurs via mixing with one of these Ta-ligand modes. The peak at  $625\text{ cm}^{-1}$  ( $^{15}\Delta = -22\text{ cm}^{-1}$ ) was identified as the asymmetric  $Ta_1-N_2$  stretching band. The symmetric  $Ta_1-N_2$  mode was found to be split into two bands at  $487$  and  $469\text{ cm}^{-1}$  due to mixing with terminal ligand modes. These features exhibit  $^{15}N_2$  isotope shifts of  $5$  and  $6\text{ cm}^{-1}$ , which fits quite well to a calculated isotope shift of  $12\text{ cm}^{-1}$  of the pure vibration. Finally, the out-of-plane mode of the  $Ta_2N_2$  moiety was identified at  $442\text{ cm}^{-1}$  ( $^{15}\Delta = -10\text{ cm}^{-1}$ ). The high intensities of the  $Ta_2N_2$  modes in the Raman spectra indicate that these modes are subject to a pronounced resonance enhancement with respect to the  $N_2$ -to-Ta CT transition at 500 nm.

To evaluate the vibrational data, a QCB-NCA was applied. This procedure is useful for the treatment of large molecules with low symmetry, leading to a large number of different off-diagonal elements that cannot be neglected. Force constants that are not necessary for the description of the obtained frequencies are fixed at their theoretical values derived by the DFT calculation. Since most values are fixed and only a few force constants that are of further interest are fitted to the experimental data, this method can handle even large molecules. Thus, the information obtainable from DFT is exploited to a maximum degree and the problems associated with the application of empirical force fields in normal coordinate analyses are avoided.

The agreement between the observed frequencies and those resulting from QCB-NCA is good, which indicates that this procedure properly accounts for the vibrational properties of **1**. The force constant for the N–N bond is calculated to be  $2.430\text{ mdyn \AA}^{-1}$ . This reflects the strong activation of the dinitrogen in **1** compared to free  $N_2$  ( $22.42\text{ mdyn \AA}^{-1}$ ).<sup>23</sup> In fact, this force constant is even lower than that of free hydrazine ( $4.3\text{ mdyn \AA}^{-1}$ ).<sup>24</sup> However, the side-on end-on coordination mode does not produce the strongest activated  $N_2$  unit as evident from the N–N force constant for the side-on  $N_2$ -coordinated complex **2**, which was calculated to be  $1.53\text{ mdyn \AA}^{-1}$ .<sup>16</sup> The force constant for the end-on-coordinated  $Ta_2-N_5$  bond,  $r_{TaN3}$ , was calculated to be  $2.517\text{ mdyn \AA}^{-1}$ , whereas the force constants for the side-on coordinating Ta–N bonds  $r_{TaN1}$  and  $r_{TaN2}$  were determined to be  $1.291$  and  $0.917\text{ mdyn \AA}^{-1}$ , respectively. The relative magnitudes of these force constants ( $r_{TaN3} > r_{TaN1} > r_{TaN2}$ ) are in line with the relative Ta–N bond lengths:  $Ta_2-N_5$  ( $1.887\text{ \AA}$ )  $<$   $Ta_1-N_6$  ( $1.966\text{ \AA}$ )  $<$   $Ta_1-N_5$  ( $2.139\text{ \AA}$ ). The force constant for the out-of-plane mode  $\gamma_{N-N}$  was calculated to be  $0.482\text{ mdyn \AA}^{-1}$ . Finally, the force constants for the  $Ta_2H_2$  moiety lie in the range  $0.688$ – $0.427\text{ mdyn \AA}^{-1}$ .

The vibrational spectroscopic data and the force constants suggest that the degree of  $N_2$  activation in **1** is intermediate

(23) Fadini, A. *Molekülkraftkonstanten-Zur Theorie und Berechnung der Konstanten der potentiellen Energie der Moleküle*; Steinkopff Verlag: Darmstadt, 1976.

(24) Catalano, E.; Sanborn, R. H.; Frazer, J. W. *J. Chem. Phys.* **1963**, *38*, 2265.

between end-on and side-on complexes and actually closer to the former than the latter systems. With an N–N distance of 1.32 Å and an N–N stretching frequency of 1165 cm<sup>-1</sup>, the activation of N<sub>2</sub> in compound **1** is slightly above the range found in end-on N<sub>2</sub>-bridged complexes ( $r_{\text{NN}} = 1.2\text{--}1.3$  Å,  $\nu_{\text{NN}} = 1200\text{--}1300$  cm<sup>-1</sup>).<sup>11,12</sup> In fact, there is one end-on bridged complex that even has a longer N–N bond length than **1**.<sup>25</sup> On the other hand, **1** has a significantly less activated N<sub>2</sub> ligand than found in side-on N<sub>2</sub>-bridged dinitrogen complexes, which have much longer N–N bonds (1.4–1.5 Å) and lower N–N stretching frequencies (700–800 cm<sup>-1</sup>).<sup>13–15</sup> This intermediate position of the  $\eta^1:\eta^2$ -bridged structure is also evident from an analysis of the electronic structure of **1**. In particular, the NPA charge analysis gives an overall electronic charge of –1.08 of N<sub>2</sub>, which is equally distributed over the two nitrogen atoms, fairly close to the value found in end-on-bridged dinitrogen complexes (–0.84 for the complex [(Me<sub>3</sub>Si)<sub>2</sub>NTiCl(TMEDA)]<sub>2</sub>( $\mu$ - $\eta^1:\eta^1$ -N<sub>2</sub>) (TMEDA = tetramethylethylenediamine)),<sup>26,27</sup> but significantly lower than found in side-on-bridged N<sub>2</sub> complexes (–1.82 for complex **2**).<sup>16</sup> The symmetric charge distribution found for the N<sub>2</sub> ligand in **1**, however, does not explain that reactions with electrophiles appear to occur exclusively at N6, the terminal N atom. To understand this result, the electronic structure of **1** has to be considered in more detail.

In Part 3 of the Results and Analysis section, bonding between dinitrogen and transition-metal centers has been analyzed in terms of interactions between the Ta d orbitals and the MOs of dinitrogen, i.e.,  $p_\sigma$ , the N–N bonding orbital,  $\pi_h$  and  $\pi_v$ , the in-plane and out-of-plane N–N  $\pi$ -bonding orbitals, and  $\pi_h^*/\pi_v^*$ , the in-plane/out-of-plane N–N  $\pi$ -antibonding orbitals. Interestingly, the two  $\pi$  orbitals have been found to have strong contributions at atom N5, which mediates bonding to Ta2 as well as bridging between Ta1 and Ta2, whereas the two  $\pi^*$  orbitals have been found to have strong contributions at N6, which is bound to Ta1 (see Figure 11 and Table 4). It can be shown that these orbital polarizations are induced by the end-on bonding of the dinitrogen ligand to Ta2 (see Figure 13 for one set of  $\pi$  and  $\pi^*$  orbitals, h or v): at lowest in energy is the bonding combination between the Ta2 d $\pi$  orbital and the N<sub>2</sub>  $\pi$  orbital, which is admixed by a bonding combination between d $\pi$  and the N<sub>2</sub>  $\pi^*$  orbital; this gives a strong contribution at N5 and a weak contribution at N6 in the resulting MO. Population of this orbital corresponds to a charge transfer from N<sub>2</sub> to the metal, the charge mostly being withdrawn from N6. At intermediate energy (approximately the energy of the metal d orbitals) is a superposition of a bonding combination between the metal d $\pi$  and dinitrogen  $\pi^*$  orbital and an antibonding combination between the metal d $\pi$  and dinitrogen  $\pi$  orbital; this gives a near-cancellation of phases at N5 and an enhancement of phases at N6. Occupation of this orbital therefore corresponds to a charge transfer from the metal to N<sub>2</sub> (back-bonding), which mostly goes to N6, the terminal N atom. At highest energy are the antibonding combinations of  $\pi$  and  $\pi^*$  with the metal d $\pi$  orbital which are unoccupied.

The described picture, which holds for all end-on terminally coordinated N<sub>2</sub> complexes, is modified in the case of **1** by side-

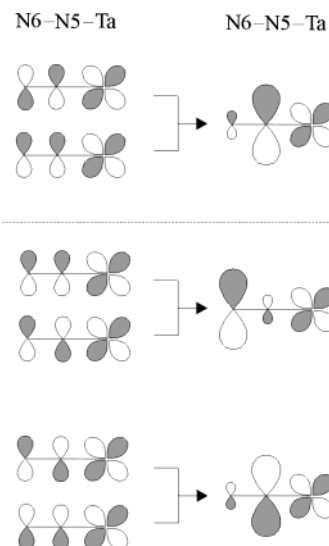


**Figure 13.** Bonding considerations of the Ta- $\eta^1$ -N<sub>2</sub> moiety.

on bonding of the N<sub>2</sub> unit to a second Ta center Ta1, at approximately a right angle to the end-on Ta2–N<sub>2</sub> unit. While this transfers additional charge to the N<sub>2</sub> ligand and further elongates the N–N bond, it does not induce any asymmetry either in orbital composition or in charge distribution of this ligand. As the N–N  $\sigma$ -bonding orbital  $p_\sigma$  contains approximately equal contributions from N5 and N6 (Table 4) and the electronic charges at N5 and N6 are found to be equal (vide supra), the opposite polarizations of the N<sub>2</sub> unit induced by  $\pi$  and  $\pi^*$  obviously cancel in the case of complex **1**. However, the large orbital contributions of N6 to the two  $\pi^*$  orbitals (the HOMO-1 and the HOMO of **1**) are important for the reactivity of this complex toward electrophiles, as they make N6 the favorite site for electrophilic attack, due to good orbital overlap with the LUMO of the electrophile.

In summary, a complete understanding of the vibrational and electronic structure of the Ta<sub>2</sub>N<sub>2</sub> core of ([NPN]Ta( $\mu$ -H))<sub>2</sub>( $\mu$ - $\eta^1:\eta^2$ -N<sub>2</sub>), **1**, has been achieved. The extent of the activation has been analyzed, and its reactivity with electrophilic reagents has been rationalized. Further spectroscopic and theoretical studies on derivatives of **1** resulting from reactions with electrophiles should allow theoretical conclusions regarding the mechanism of the electrophilic attack and subsequent transformations of the complex including cleavage of the N–N bond.

## Experimental Section

**1. Synthesis of **1** and Its Isotopomers.** ([NPN]Ta( $\mu$ -H))<sub>2</sub>( $\mu$ - $\eta^1:\eta^2$ -N<sub>2</sub>), ([NPN]Ta( $\mu$ -D))<sub>2</sub>( $\mu$ - $\eta^1:\eta^2$ -N<sub>2</sub>), and ([NPN]Ta( $\mu$ -H))<sub>2</sub>( $\mu$ - $\eta^1:\eta^2$ -<sup>15</sup>N<sub>2</sub>) were all prepared according to literature procedures.<sup>17</sup>

**2. IR Spectroscopy.** Middle infrared (MIR) spectra were obtained from RbI pellets using a Mattson Genesis Type I spectrometer. Far-infrared (FIR) spectra were obtained from RbI pellets using a Bruker IFS 66 FTIR spectrometer. Both instruments were equipped with a Cryogenics helium cryostat. The spectra were recorded at 10 K, and the resolution was set to 2 cm<sup>-1</sup>.

**3. Resonance Raman Spectroscopy.** Resonance Raman spectra were measured using a Dilor XY-Raman spectrograph with triple monochromator and CCD detector. An argon/krypton mixed gas laser with a maximum power of 5 W was used for excitation. The spectra were recorded with an excitation wavelength of 568.2 nm. The samples were measured as RbI pellets and cooled to 10 K with a helium cryostat. Spectral band-pass was set to 2 cm<sup>-1</sup>.

(25) Berno, P.; Gambarotta, S. *Organometallics* **1995**, *14*, 2159–2161.

(26) Lehnert, N. Ph.D. Thesis, Johannes Gutenberg-Universität Mainz (Germany), 1999.

(27) Duchateau, R.; Gambarotta, S.; Beydoun, N.; Bensimon, C. *J. Am. Chem. Soc.* **1991**, *113*, 8986.

**4. UV–Vis Spectroscopy.** The UV–vis spectrum in solution (diethyl ether) was recorded on an Analytik Jena Specord S 100 spectrometer. The resolution was set to 1 nm. The other UV–vis spectrum was obtained on neat compound pressed between sapphire windows. The spectrum was recorded at 10 K using a Varian Cary 5 UV/vis/NIR spectrometer equipped with a CTI cryocooler.

**5. Normal Coordinate Analysis.** Normal coordinate calculations were performed using the QCPE computer program 576.<sup>28</sup> The calculations were based on a general valence force field, and the force constants were refined using the nonlinear optimization routine of the simplex algorithm according to Nelder and Mead.<sup>29</sup> Only selected force constants were refined due to the QCB-NCA procedure (see Results and Analysis section).

**6. Density Functional Theory Calculations.** Spin-restricted DFT calculations using Becke's three-parameter hybrid functional with the correlation functional of Lee, Yang, and Parr (B3LYP)<sup>30–32</sup> were performed for the singlet ground state of a simplified model of complex **1**. The LANL2DZ basis set was used for the calculation, which applies Dunning/Huzinaga full double- $\zeta$  (D95) basis functions<sup>33</sup> on the first row and Los Alamos effective core potentials plus DZ functions on all other atoms.<sup>34,35</sup> Convergence was reached when the relative change in the density matrix between subsequent iterations was less than  $1 \times$

$10^{-8}$  for single points and optimizations. Charges were analyzed using the natural bond orbital (NBO) formalism.<sup>36–39</sup> All computational procedures were used as they are implemented in the Gaussian 98 package.<sup>40</sup> Wave functions were plotted using the visualization program Gaussview 2.1. The force constants in internal coordinates were extracted from the Gaussian output using the program Redong.<sup>22</sup>

**Acknowledgment.** F.T. thanks DFG TU58-12 and FCI (Fonds der Chemischen Industrie) for financial support. F.S. thanks U. Cornelissen for assistance with the spectroscopic measurements. M.D.F. and B.A.M. thank NSERC of Canada for funding.

**Supporting Information Available:** Density functional theory calculation results for model complex **1** (PDF). This material is available free of charge via the Internet at <http://pubs.acs.org>.

JA036997Y

(28) Peterson, M. R.; McIntosh, D. F. QCPE program 576, Quantum Chemistry Program Exchange, Department of Chemistry, Indiana University, Bloomington, IN, 1988.

(29) Nelder, J. A.; Mead, R. *Comput. J.* **1965**, *7*, 308.

(30) Becke, A. D. *Phys. Rev. A* **1988**, *38*, 3098.

(31) Becke, A. D. *J. Chem. Phys.* **1993**, *98*, 1372.

(32) Becke, A. D. *J. Chem. Phys.* **1993**, *98*, 5648.

(33) Dunning, T. H., Jr.; Hay, P. J. In *Modern Theoretical Chemistry*; Schaefer, H. F., III, Ed.; Plenum: New York, 1976.

(34) Hay, P. J.; Wadt, W. R. *J. Chem. Phys.* **1985**, *82*, 270 and 299.

(35) Wadt, W. R.; Hay, P. J. *J. Chem. Phys.* **1985**, *82*, 284.

(36) Foster, J. P.; Weinhold, F. *J. Am. Chem. Soc.* **1980**, *102*, 7211.

(37) Rives, A. B.; Weinhold, F. *Int. J. Quantum Chem. Symp.* **1980**, *14*, 201.

(38) Reed, A. E.; Weinstock, R. B.; Weinhold, F. *J. Chem. Phys.* **1985**, *83*, 735.

(39) Reed, A. E.; Curtiss, L. A.; Weinhold, F. *Chem. Rev.* **1988**, *88*, 899.

(40) Frisch, M. J.; Trucks, G. W.; Schlegel, H. B.; Scuseria, G. E.; Robb, M. A.; Cheeseman, J. R.; Zakrzewski, V. G.; Montgomery, J. A., Jr.; Stratmann, R. E.; Burant, J. C.; Dapprich, S.; Millam, J. M.; Daniels, A. D.; Kudin, K. N.; Strain, M. C.; Farkas, O.; Tomasi, J.; Barone, V.; Cossi, M.; Cammi, R.; Mennucci, B.; Pomelli, C.; Adamo, C.; Clifford, S.; Ochterski, J.; Petersson, G. A.; Ayala, P. Y.; Cui, Q.; Morokuma, K.; Salvador, P.; Dannenberg, J. J.; Malick, D. K.; Rabuck, A. D.; Raghavachari, K.; Foresman, J. B.; Cioslowski, J.; Ortiz, J. V.; Baboul, A. G.; Stefanov, B. B.; Liu, G.; Liashenko, A.; Piskorz, P.; Komaromi, I.; Gomperts, R.; Martin, R. L.; Fox, D. J.; Keith, T.; Al-Laham, M. A.; Peng, C. Y.; Nanayakkara, A.; Challacombe, M.; Gill, P. M. W.; Johnson, B.; Chen, W.; Wong, M. W.; Andres, J. L.; Gonzalez, C.; Head-Gordon, M.; Replogle, E. S.; Pople, J. A. *Gaussian 98*, rev. A.11; Gaussian, Inc.: Pittsburgh, 2001.